Monthly Notices
of the
ROYAL ASTRONOMICAL SOCIETY

MNRAS **467,** 3347–3360 (2017)
Advance Access publication 2017 February 24

doi:10.1093/mnras/stx291

Supernova progenitors, their variability and the Type IIP Supernova ASASSN-16fq in M66

C. S. Kochanek,[1,2]★ M. Fraser,[3] S. M. Adams,[4] T. Sukhbold,[1,2] J. L. Prieto,[5,6] T. Müller,[6,7] G. Bock,[8] J. S. Brown,[1] Subo Dong,[9] T. W.-S. Holoien,[1] R. Khan,[10] B. J. Shappee[11]† and K. Z. Stanek[1,2]

[1]*Department of Astronomy, The Ohio State University, 140 West 18th Avenue, Columbus, OH 43210, USA*
[2]*Center for Cosmology and AstroParticle Physics, The Ohio State University, 191 W. Woodruff Avenue, Columbus, OH 43210, USA*
[3]*Institute of Astronomy, University of Cambridge, Madingley Rd, Cambridge CB3 0HA, UK*
[4]*Cahill Center for Astrophysics, California Institute of Technology, Pasadena, CA 91125, USA*
[5]*Núcleo de Astronomía de la Facultad de Ingeniería, Universidad Diego Portales, Av. Ejército 441, Santiago, Chile*
[6]*Millennium Institute of Astrophysics, Santiago 7591245, Chile*
[7]*Instituto de Astrofísica, Pontifica Universidad Católica de Chile, Av. Vicuña Mackenna 4860, 782-0436 Macul, Santiago, Chile*
[8]*Runaway Bay Observatory, 1 Lee Road, Runaway Bay, Queensland 4216, Australia*
[9]*Kavli Institute for Astronomy and Astrophysics, Peking University, Yi He Yuan Road 5, Hai Dian District, Beijing 100871, China*
[10]*Department of Astronomy, Box 351580, University of Washington, Seattle, WA 98195, USA*
[11]*Carnegie Observatories, 813 Santa Barbara Street, Pasadena, CA 91101, USA*

Accepted 2017 January 31. Received 2017 January 22; in original form 2016 August 31

ABSTRACT

We identify a pre-explosion counterpart to the nearby Type IIP supernova ASASSN-16fq (SN 2016cok) in archival *Hubble Space Telescope* data. The source appears to be a blend of several stars that prevents obtaining accurate photometry. However, with reasonable assumptions about the stellar temperature and extinction, the progenitor almost certainly had an initial mass $M_* \lesssim 17\,\mathrm{M}_\odot$, and was most likely in the mass range of $M_* = 8$–$12\,\mathrm{M}_\odot$. Observations once ASASSN-16fq has faded will have no difficulty accurately determining the properties of the progenitor. In 8 yr of Large Binocular Telescope (LBT) data, no significant progenitor variability is detected to rms limits of roughly 0.03 mag. Of the six nearby supernova (SN) with constraints on the low-level variability, SN 1987A, SN 1993J, SN 2008cn, SN 2011dh, SN 2013ej and ASASSN-16fq, only the slowly fading progenitor of SN 2011dh showed clear evidence of variability. Excluding SN 1987A, the 90 per cent confidence limit implied by these sources on the number of outbursts over the last decade before the SN that last longer than 0.1 yr (full width at half-maximum) and are brighter than $M_R < -8$ mag is approximately $N_{\rm out} \lesssim 3$. Our continuing LBT monitoring programme will steadily improve constraints on pre-SN progenitor variability at amplitudes far lower than achievable by SN surveys.

Key words: stars: massive – supernovae: general – supernovae: individual: SN 2016cok – galaxies: individual: M 66.

1 INTRODUCTION

At the end of their lives, all massive ($\gtrsim 8\,\mathrm{M}_\odot$) stars must undergo core collapse once their iron cores become too massive to be stable. In most cases, this leads to a supernova (SN) explosion, probably driven by some combination of neutrino heating and the effects of turbulence and convection (see the recent review by Müller 2016 and, for example, recent results by Couch & Ott 2015; Dolence, Burrows & Zhang 2015; Wongwathanarat, Müller & Janka 2015). The visible properties of the successful SNe then depend on the degree of mass-loss, ranging from Type IIP SN that have retained most of their hydrogen envelopes, to Type Ic SN that appear to have been stripped even of helium (e.g. Filippenko 1997). The mass-loss is controlled by some combination of intrinsic effects such as winds and extrinsic effects, such as binary mass transfer (see the review by Smith 2014).

There is no strong requirement that more than roughly 50 per cent of core collapses lead to successful SN (e.g. neutrino backgrounds: Lien, Fields & Beacom 2010; star formation rates: Horiuchi et al. 2011; nucleosynthesis: Brown & Woosley 2013; Clausen,

★ E-mail: ckochanek@astronomy.ohio-state.edu
† Hubble, Carnegie-Princeton Fellow.

Piro & Ott 2015) and a 10–30 per cent fraction of failed SN producing black holes without a dramatic external explosion is both expected in many modern analyses of the 'explodability' of stars (e.g. Ugliano et al. 2012; O'Connor & Ott 2013; Pejcha & Thompson 2015; Ertl et al. 2016; Sukhbold et al. 2016) and would provide a natural explanation of the compact remnant mass function (Kochanek 2014; Clausen et al. 2015; Kochanek 2015). Indeed, scenarios for the recent gravitational wave detection of a merging black hole binary (Abbott et al. 2016) all invoke at least one failed SN (e.g. Belczynski et al. 2016; Woosley 2016).

A powerful means of probing these issues is to work out the mapping between successful SNe and their progenitor stars. This is a challenging observational programme (see the reviews by Smartt 2009 and Smartt 2015) that has slowly been carried out over the last 20 yr (e.g. Van Dyk, Li & Filippenko 2003; Smartt et al. 2004; Li et al. 2006; Elias-Rosa et al. 2009; Smartt et al. 2009; Elias-Rosa et al. 2011; Maund et al. 2011; Van Dyk et al. 2011; Fraser et al. 2012; Fraser et al. 2014). With one possible exception (Cao et al. 2013; Folatelli et al. 2016, see Eldridge et al. 2013 for a discussion of limits), all the identified progenitors are of Type II (IIP, IIL, IIb or IIn).

As first pointed out by Kochanek et al. (2008) and then better quantified by Smartt et al. (2009), there appears to be a deficit of higher mass SN progenitors. In particular, Smartt et al. (2009) identified only Type IIP progenitors with masses of $\lesssim 17\,M_\odot$, even though stars up to 25–30 $M_\odot$ are expected to explode as red supergiants with most of their hydrogen envelopes. While attempts have been made to explain this using extinction by winds (Walmswell & Eldridge 2012, but see Kochanek, Khan & Dai 2012b) or by modifying stellar evolution (e.g. Groh et al. 2013), the same problem of missing, higher mass progenitors is seen in examinations of the stellar populations near Local Group SN remnants (Jennings et al. 2014). Jerkstrand et al. (2014) also argue that no Type IIP SN have shown nucleosynthetic evidence for a higher mass ($M_* > 20\,M_\odot$) progenitor. Following the proposal of Kochanek et al. (2008), Gerke, Kochanek & Stanek (2015) and Adams et al. (2016c) have been carrying out a search for failed SN with the Large Binocular Telescope (LBT), identifying one promising candidate (see also Reynolds, Fraser & Gilmore 2015). The progenitor of this candidate for a failed SN appears to be a red supergiant in exactly the mass range missing from searches for the progenitors of successful SN (Adams et al. 2016b).

A second recent puzzle about SN progenitors is that some appear to have outbursts (Pastorello et al. 2007; Fraser et al. 2013; Mauerhan et al. 2013; Ofek et al. 2014; Ofek et al. 2016) and/or eject significant amounts of mass (see Gal-Yam 2012; Smith 2014) shortly before they explode. The most extreme mass-loss events ($\dot{M} \sim M_\odot\ \mathrm{yr}^{-1}$) likely explain the rare, superluminous Type IIn SNe (Smith & McCray 2007), but the inferred mass-loss rates are frequently $\dot{M} \gtrsim 10^{-3}\,M_\odot\ \mathrm{yr}^{-1}$, even for the normal Type IIn SNe (see e.g. Kiewe et al. 2012). The local systems known to reach such extreme mass-loss rates are the luminous blue variables (LBVs), with η Carinae as the most spectacular example (see Humphreys & Davidson 1994). The rate of η Carinae-like events is roughly 10 per cent of the SN rate (Kochanek 2011; Khan et al. 2015a,b), which is sufficient to explain the occurrence of the extreme Type IIn superluminous SN. Any association of LBV eruptions with the very late phases of stellar evolution would roughly require the typical $M_* \gtrsim 50\,M_\odot$ star to have at least one eruption in the $\sim 10^3$-yr period after carbon ignition (Kochanek 2011). On the other hand, theoretical models to explain pre-SN outbursts and Type IIn SNe have favoured mechanisms associated with the last few years, corresponding to the neon/oxygen burning phases or later (Quataert & Shiode 2012; Shiode & Quataert 2014; Smith & Arnett 2014; Woosley & Heger 2015). In this picture, massive stars must have two separate mechanisms for triggering outbursts, one to explain the LBVs and a second to explain the pre-SN outbursts.

The existence of any transients associated with the last $\lesssim 10^3$ yr (or less) of stellar life requires a causal mechanism associated with these final phases (see the discussion in Kochanek 2011). Fig. 1 shows the dependence of the final nuclear burning stages on progenitor mass for the standard, non-rotating, 12–100 $M_\odot$, solar metallicity models of Sukhbold & Woosley (2014) and Woosley & Heger (2007). We show the periods of core and shell carbon, oxygen and silicon burning – the neon burning phase is not as energetically important. The large-scale structure in Fig. 1, with the shortest timescales for intermediate masses, is driven by the rapid increase in mass-loss for the higher mass stars. The smaller scale variations in the mass-dependence of the post-carbon burning phases are due to the complex interplay of the burning phases and their consequences for structure of the stellar core (see Sukhbold & Woosley 2014 for a detailed discussion). Keep in mind, however, that these are single star evolution models, while many SN progenitors are in binaries that will interact (e.g. Sana et al. 2012) and follow modified evolutionary paths.

We illustrate the outbursts associated with Type IIn SN in Fig. 1 by SN 2009ip and the Palomar Transient Factory (PTF) sample of Type IIn SN considered by Ofek et al. (2014). SN 2009ip has an estimated progenitor mass of 50–80 $M_\odot$ (Smith et al. 2010) and showed a series of outbursts before the apparent explosion (see, e.g. Smith et al. 2010; Foley et al. 2011; Mauerhan et al. 2013; Pastorello et al. 2013; Margutti et al. 2014). For the PTF sample, the progenitor masses are unknown. PTF data are available for the last few years before the SN, as shown by the lines spanning the survey times for each SN. Ofek et al. (2014) detect five outbursts and argue that it is highly probable that all Type IIn SN experience outbursts and that many are simply missed due to the survey depth and cadence. The outbursts shown in Fig. 1 are associated with the very last phases of carbon shell burning through the early phases of oxygen shell burning. It seems probable, particularly in the case of SN 2009ip, that outbursts cannot be restricted to the time period after the initiation of core oxygen burning. As a contrast, if the eruption mechanism of LBVs had any correlation with these last phases, it would have to be associated with the carbon burning phase, as illustrated in Fig. 1 by the 1840 and 1655 outbursts of η Car and P Cygni (see Humphreys & Davidson 1994).

Broadly speaking, there are two possible scenarios associated with these pre-SN transients. The first option is that only the high-amplitude events seen in the SN surveys or implied by the Type IIn SNe exist and they are associated with a very narrow range of progenitor parameter space (e.g. mass, metallicity, rotation). The second option is that the outburst mechanism is relatively generic, and the existing events simply represent the high-amplitude tail of a much broader distribution. Unfortunately, the existing systematic searches for outbursts (e.g. Ofek et al. 2014; Bilinski et al. 2015; Strotjohann et al. 2015) are all part of searches for SNe and essentially cannot detect significantly lower amplitude transients.

Like building the mapping between SN and progenitors, building the mapping between pre-SN outbursts and progenitors requires surveys of much greater sensitivity than searches for SN. Unfortunately, where data deep enough to observe progenitors are already rare, having multiple epochs of such data to study progenitor variability is still rarer. At present, such data only exist for the progenitors of SN 1987A (see Plotkin & Clayton 2004 and references

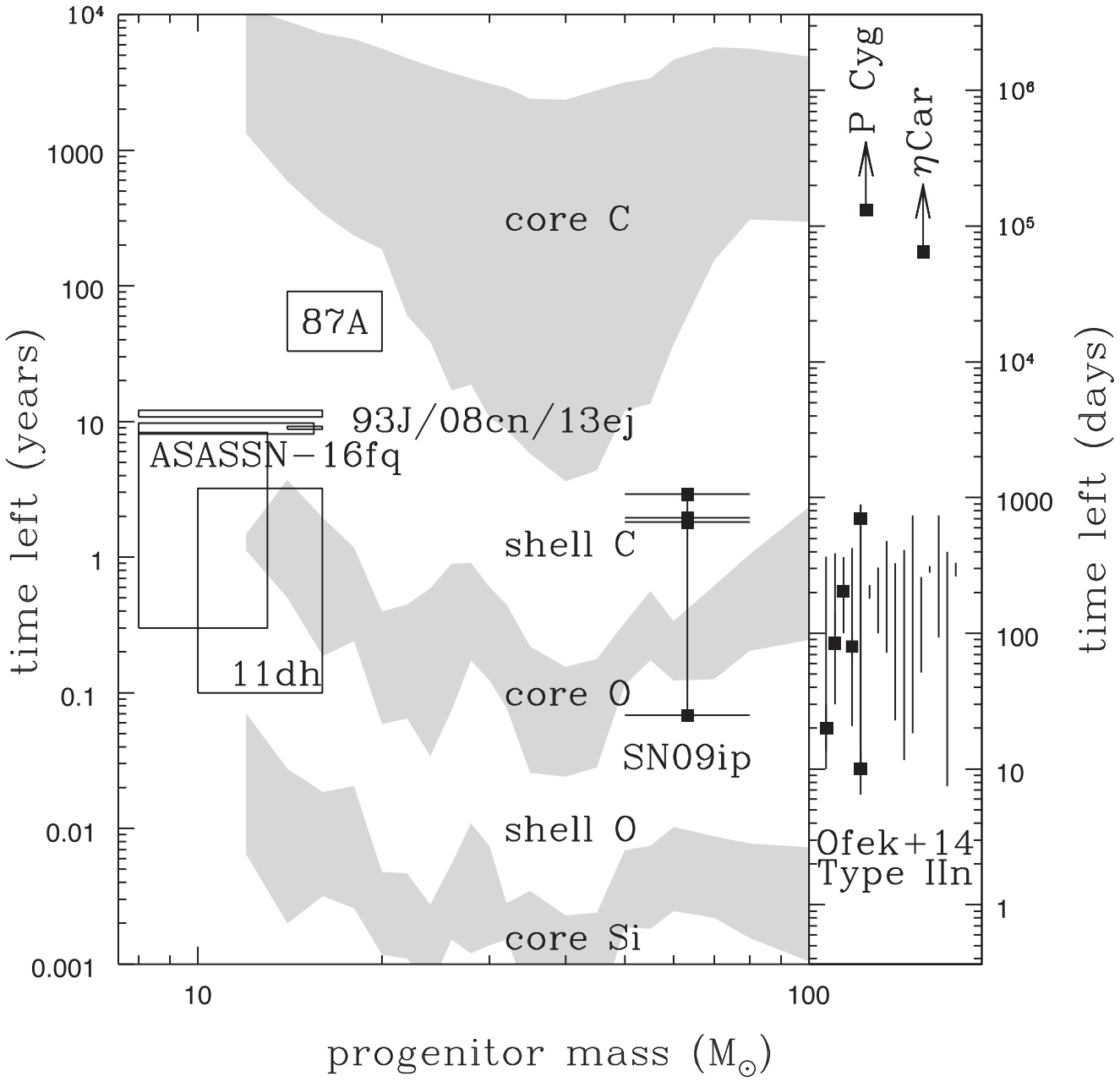

Figure 1. Final nuclear burning stages as a function of progenitor mass based on the standard, non-rotating, 12–100 $M_\odot$, solar metallicity models of Sukhbold & Woosley (2014) and Woosley & Heger (2007). The grey bands show, from top to bottom panel, the periods of core carbon, oxygen and silicon burning, separated by periods of shell burning. The points associated with SN 2009ip indicate the timing of its outbursts relative to its presumed explosion along with its estimated mass range. The sub-panel to the right shows 16 thin vertical lines for the (control) time periods sampled by PTF for 16 Type IIn SN, with heavy black points and lines for the time periods associated with outbursts (Ofek et al. 2014). The masses of the progenitors of these stars are unknown but they are generally assumed to be large. For comparison, the sub-panel also indicates the present-day lower limits for the 1840 and 1655 outbursts of η Car and P Cyg. The boxes at lower masses show the progenitor mass ranges and the time periods that can be surveyed for progenitor variability for SN 1987A, SN 1993J, SN 2008cn, SN 2011dh, SN 2013ej and ASASSN-16fq. For a Salpeter IMF with SN occurring in the mass range from 8 to 100 $M_\odot$, 50 per cent of SN arise from the mass range from 8 to 13.1 $M_\odot$.

therein), SN 1993J (Cohen, Darling & Porter 1995), SN 2008cn (Elias-Rosa et al. 2009; Maund et al. 2015), SN 2011dh (Szczygieł et al. 2012) and SN 2013ej (Fraser et al. 2014). These sources all have progenitor detections and mass estimates, placing them below 20 $M_\odot$. Fig. 1 shows the region of progenitor mass and remaining lifetime the data can probe. The variability constraints for SN 1987A and SN 1993J are relatively poor, and only SN 2011dh shows clear evidence for low levels of variability. All these systems are also in the $\lesssim$20 $M_\odot$ mass range suggested by Shiode & Quataert (2014) for a wave-driven mass-loss at solar metallicity, and some are likely near the $\sim$10 $M_\odot$ mass range associated with the explosive silicon burning mechanism of Woosley & Heger (2015).

Here we report on the properties of the progenitor of ASASSN-16fq (SN 2016cok). ASASSN-16fq was discovered

Table 1. *HST* photometry.

Date	Instr.	Exp. (# × s)	Src.	*F435W* (mag)	*F555W* (mag)	*F606W* (mag)	*F658N* (mag)	*F814W* (mag)
1994-12-28	WFPC2	2 × 80	All	–	–	23.639 ± 0.099	–	–
2001-02-24	WFPC2	2 × 350	All	–	–	–	–	22.225 ± 0.041
			HSC	–	–	–	–	22.302 ± 0.083
2001-03-04	WFPC2	2 × 350	All	–	23.396 ± 0.083	–	–	–
2001-11-26	WFPC2	160 + 400	All	–	–	23.160 ± 0.038	–	–
2004-12-31	ACS	2 × 600	B1	–	–	–	22.708 ± 0.081	–
			B2	–	–	–	24.356 ± 0.315	–
			B3	–	–	–	24.384 ± 0.323	–
			HSC	–	–	–	22.813 ± 0.075	–
2004-12-31	ACS	2 × 500	A1	24.149 ± 0.041	–	–	–	–
			A2	26.034 ± 0.190	–	–	–	–
			A3	26.011 ± 0.180	–	–	–	–
			A4	26.250 ± 0.210	–	–	–	–
			A5	26.189 ± 0.187	–	–	–	–
			A6	26.727 ± 0.282	–	–	–	–
			HSC	24.097 ± 0.024	–	–	–	–
2009-12-14	ACS	2 × 260	C1	–	23.899 ± 0.037	–	–	–
			C2	–	25.015 ± 0.085	–	–	–
			C3	–	25.392 ± 0.114	–	–	–
			C4	–	26.259 ± 0.233	–	–	–
			C5	–	26.889 ± 0.416	–	–	–
			C6	–	26.254 ± 0.233	–	–	–
			C7	–	26.119 ± 0.196	–	–	–
			HSC	–	23.768 ± 0.032	–	–	–
2009-12-14	ACS	2 × 260	D1	–	–	–	–	23.308 ± 0.036
			D2	–	–	–	–	23.720 ± 0.050
			D3	–	–	–	–	24.224 ± 0.073
			D4	–	–	–	–	24.991 ± 0.133
			HSC	–	–	–	–	22.721 ± 0.022
2013-11-29	WFC3	3 × 373	E1	–	24.158 ± 0.028	–	–	–
			E2	–	25.202 ± 0.064	–	–	–
			E3	–	25.967 ± 0.108	–	–	–
			E4	–	26.515 ± 0.160	–	–	–
2013-11-29	WFC3	3 × 373	E1	–	–	–	–	23.204 ± 0.033
			E2	–	–	–	–	23.919 ± 0.060
			E3	–	–	–	–	25.044 ± 0.139
			E4	–	–	–	–	24.140 ± 0.064

The detectors for the WFPC2, ACS and WFC3 instruments were WF3, WFC1 and UVIS2, respectively. The WFPC2/WF3 photometry encompasses 'All' of the sources. For WFPC2/WF3 (ACS/WFC1), the HSC AB TotMag (MagAp2) results were converted to Vega magnitudes.

(Bock et al. 2016) in M66 (NGC 3627) by the All-Sky Automated Survey for Supernovae (ASAS-SN, Shappee et al. 2014) on 2016 May 28 and was spectroscopically classified as a Type IIP SN (Zhang et al. 2016). There are multiple epochs of *Hubble Space Telescope* (*HST*) data because of the debated transient SN 1997bs (Van Dyk et al. 2000; Smith et al. 2011; Kochanek, Szczygieł & Stanek 2012a; Adams & Kochanek 2015) and the Type IIL SN 2009hd (Elias-Rosa et al. 2011; Tinyanont et al. 2016). It is also one of the galaxies monitored as part of the search for failed SNe with the LBT (Kochanek et al. 2008; Gerke et al. 2015; Adams et al. 2016c), allowing a deep search for progenitor variability over its last 8 yr (see Fig. 1). In Section 2, we identify and describe the progenitor, primarily based on archival *HST* data, to make a rough estimate of its luminosity and initial mass. In Section 3, we search for variability from the progenitor using the data from the LBT. We discuss the results in Section 4, focusing on an extended discussion of SN progenitor variability. Following Gerke et al. (2015), we adopt a distance of 10.62 Mpc from Kanbur et al. (2003) and a Galactic extinction of $E(B-V) = 0.03$ mag from Schlafly & Finkbeiner (2011).

2 IDENTIFICATION AND PROPERTIES OF THE PROGENITOR

The region including ASASSN-16fq was observed by *HST* on 1994 December 28 (WFPC2/*F606W*, GO-54456, PI Illingworth), 2011 November 26 (WFPC2/*F606W*, GO-8597, PI Regan), February 24 and 2001 March 4 (WFPC2/*F555W* and *F814W*, GO-8602, PI Filippenko), 2004 December 30/31 (ACS/*F658N* and *F435W*, GO-10402, PI Chandar), 2009 December 14 (ACS/*F555W* and *F814W*, GO-11575, PI Van Dyk) and 2013 November 28 (WFC3/UVIS/*F555W* and *F814W*, GO-13477, PI Kochanek). These data are summarized in Table 1. The region has also been observed multiple times by *Spitzer* at 3.6 and 4.5 μm (programmes 159, 10001 and 10136/11063; PIs Kennicutt, Kochanek and Kasliwal, respectively).

In order to determine the position of the SN in the *HST* images, we obtained new LBT data including the SN consisting of 24 five-second *R*-band exposures with a 1.05 arcsec full width at half-maximum (FWHM) and a nominal *R*-band depth when combined of roughly 24.7 mag (S/N ≃ 5). We identified 39 sources in common between the combined LBT image and the pipeline, drizzled,

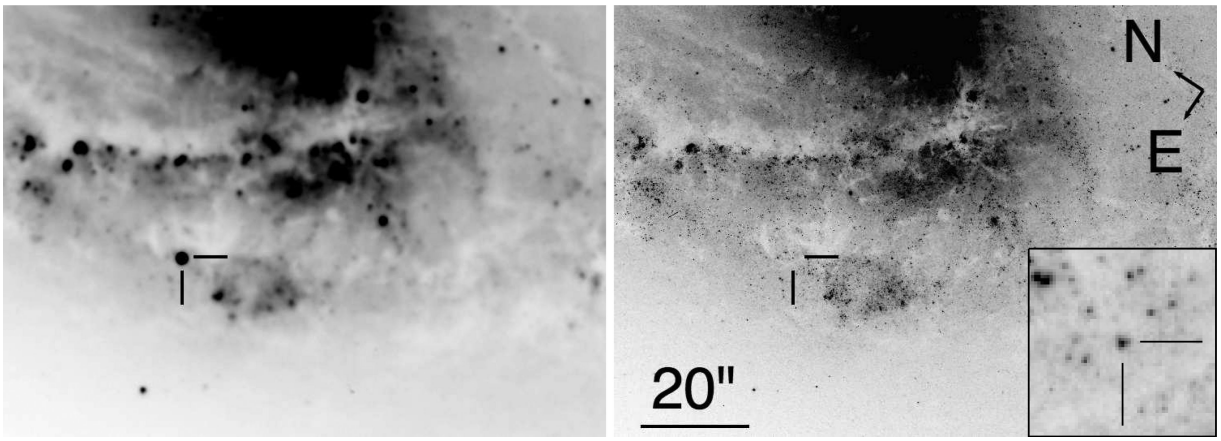

Figure 2. Identification of a progenitor candidate for ASASSN-16fq. The left-hand panel shows an image of the SN taken with LBT, aligned to the pre-explosion *HST* ACS/WFC *F814W* image shown in the right-hand panel. The position of the SN is indicated in both panels. The inset in the right, pre-explosion panel shows a 30 arcsec × 3.0 arcsec region centred on the progenitor candidate, with the derived SN position indicated.

CTE-corrected (charge transfer efficiency) ACS/WFC *F814W HST* image taken on 2009 December 14. A pixel coordinate transformation allowing for rotation, translation, independent x and y pixel scalings and second-order x^2, xy and y^2 terms to account for distortions (24 coefficients in total) led to a geometric transformation with root mean square (rms) errors in the x and y *HST* pixel axes of 0.164 and 0.169 LBT pixels, respectively. The position of the SN in the LBT image was measured using three different centring algorithms that agreed to $\lesssim$0.02 LBT pixels (pixel scale 0.226 arcsec). The resulting estimate of the pixel position of the SN on the *F814W* image is (1658.047 ± 0.734, 2014.933 ± 0.757). Fig. 2 shows the LBT image with the SN and the same region in the pre-explosion *HST* image along with an inset showing a 3.0 arcsec^2 region centred on the estimated position of the progenitor. A source is readily apparent at this position.

The pixel coordinates of this pre-explosion source are measured to be (1657.612 ± 0.094, 2014.856 ± 0.048) using the average results of three different centring algorithms in IRAF PHOT. This is offset from our estimated position of the SN by (0.435, 0.077) ACS pixels, or 0.022 arcsec in total. Thus, the SN and our progenitor candidate have formally coincident positions, given their respective uncertainties. However, this source also appears to be an extended blend of several stars, with a FWHM of 3 pixels instead of the ∼2 pixels found for nearby point sources. This proves to be a considerable complication for our photometric measurements.

For photometry, we used HSTPHOT for the WFPC2 images and DOLPHOT for the ACS and WFC3 images (Dolphin 2000). HSTPHOT is designed specifically for point spread function (PSF)-fitting photometry on WFPC2 images, while DOLPHOT is a more general version of HSTPHOT that can also handle ACS and WFC3 data. ACS, WFC3 and WFPC2 all have different pixel scales, and the observations summarized in Table 1 were taken with a range of orientations and depths. Hence, it is difficult to directly compare observations taken with each of these cameras, particularly when the decomposition of the blended sources is not unique. The photometric results are reported in Table 1 along with any magnitudes for the source available from the Hubble Source Catalogue (HSC, Whitmore et al. 2016) for comparison. All the reported magnitudes are in the Vega system, with appropriate transformations from the AB magnitudes used by the HSC.

The WFPC2 images were obtained with the WF3 detector, which has a pixel scale of 0.1 arcsec that grossly undersamples the PSF.

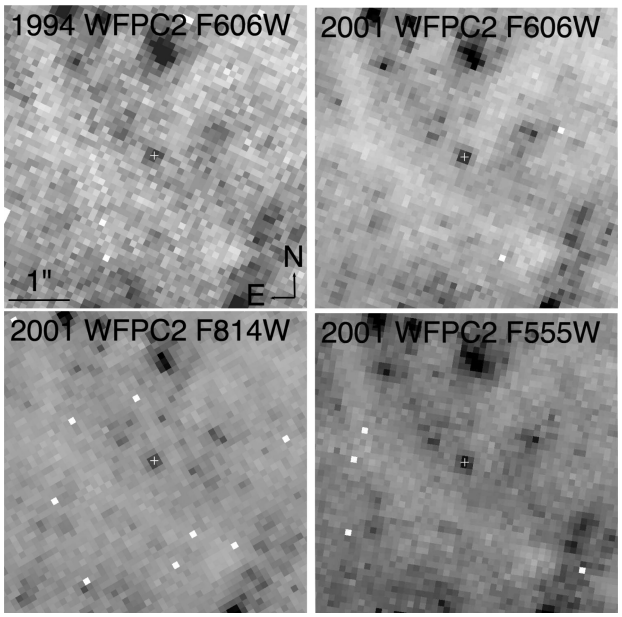

Figure 3. WFPC2 images (5.0 arcsec^2, north up) from 2001 centred on the candidate progenitor. The progenitor candidate is marked by the yellow cross. The white squares are bad pixels.

The 1994 images were very shallow and there was a slight (∼2 pix) offset between the two exposures, so we ran HSTPHOT on each frame individually. For the WFPC2 data from 2001, there was no dithering between the exposures, so we combined the two images available for each filter. Cosmic rays were rejected using the paired exposures for each pointing. HSTPHOT was run using its recommended parameters, performing PSF-fitting photometry with a detection threshold of 3.5σ, and simultaneously refitting the sky background (option 512). Aperture corrections were derived from the data and applied to the measured magnitudes along with standard CTE corrections.

In all of the WFPC2 images, the progenitor candidate was detected as a single source, as shown in Fig. 3. The 1994 and 2001 *F606W* magnitudes differ by almost 0.5 mag despite using identical settings for HSTPHOT. If we take five nearby sources with *F606W* ∼ 22 mag, we find that the sources all appear to be brighter in 2001 by 0.15–0.35 mag. The cause of the discrepancy is unclear,

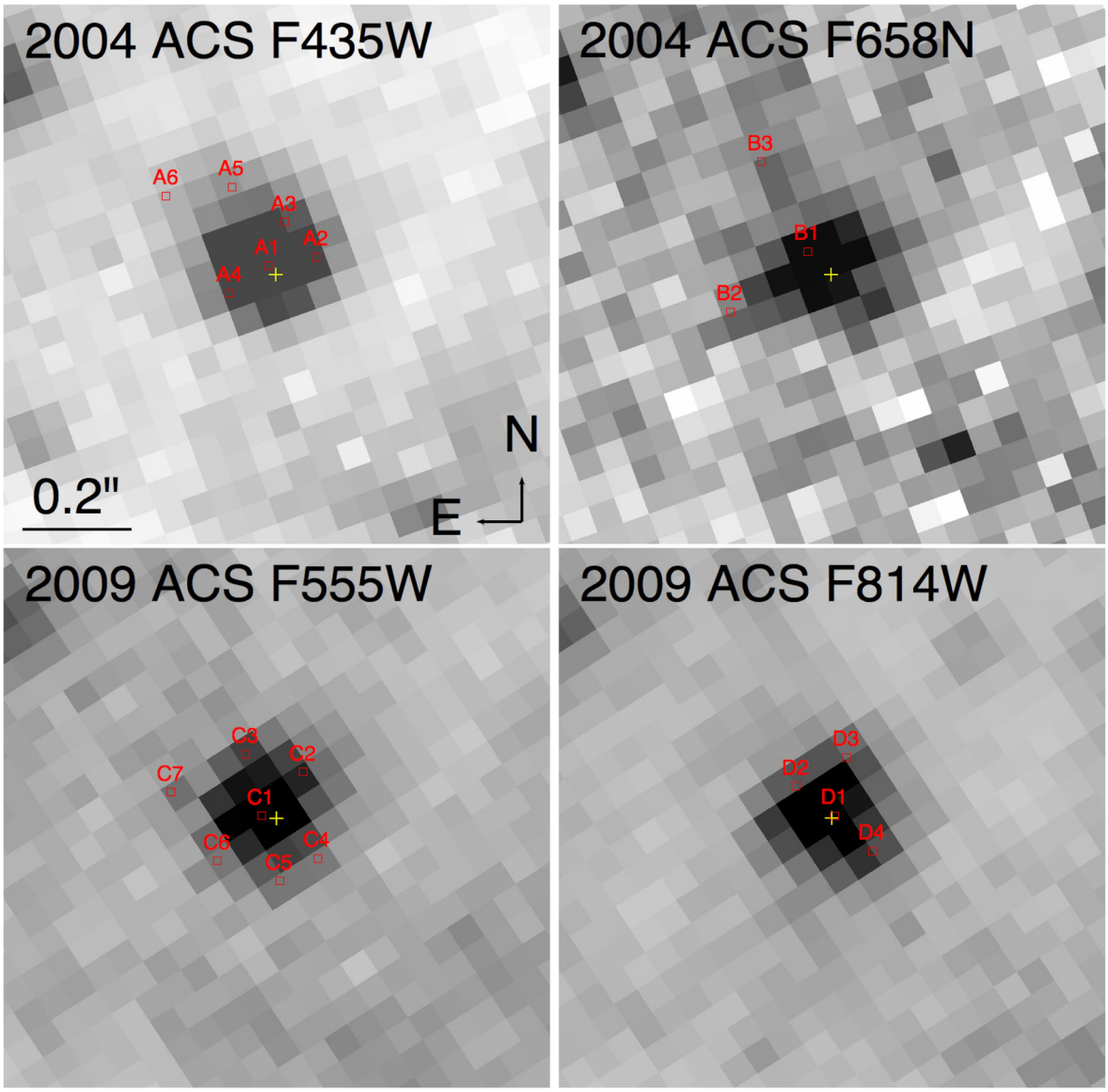

Figure 4. ACS images (1.0 arcsec^2, north up) from 2004 (*F435W* and *F658N*, top panel) and 2009 (*F555W* and *F814W*, bottom panel) centred on the estimated position of ASASSN-16fq (yellow cross). The labelled red squares show the positions of DOLPHOT sources reported in Table 1 where the central source (A1-D1) is the brightest.

although the 1994 exposures were significantly shallower and have lower backgrounds that would worsen the effects of CTE. We applied the HOTPANTS difference imaging package to the two *F606W* epochs and found no significant residuals, indicating that there was no significant variability associated with the source. We will not consider the 1994 data further. The HSC had an estimate for the source flux in the 2001 *F814W* image, and the *HST* magnitude was consistent with our photometry to <0.1 mag.

The ACS images were analysed with DOLPHOT. The drizzled ACS reference image (file type `_drc`) for each filter was used to identify sources, while photometric measurements were performed on the individual, undrizzled, `_flc` files. Both file types are corrected for CTE losses, so no CTE corrections were applied to the measured magnitudes. The pipeline-reduced 2004 ACS `_flc` files did not have a cosmic-ray mask in their data quality extension. We processed these files with ASTRODRIZZLE to derive a cosmic-ray mask before carrying out the remainder of the analysis. The DOLPHOT parameters, including the choice of aperture radius, were matched to those of the ANGST survey (Dalcanton et al. 2009). We used a large 8-pixel aperture, fitting each source, its neighbours and the background simultaneously. We used a 3σ source detection threshold and set the `force=1` parameter to force all objects to be fit as point sources. For the *F658N* image, DOLPHOT failed to detect enough sources to align the two `_flt` images to the drizzled *F658N* reference image. Here we measured the positions of many point-like sources common to each image within IRAF, and used ACSFITDISTORT within DOLPHOT to align the frames. The location of the SN in each of the images was found by aligning them to the 2009 *F814W* image that was used to identify the progenitor.

DOLPHOT splits the flux from the source at the progenitor position into a number of sources, which is not surprising given that that its FWHM is broader than other nearby, point-like sources. If we disable the `force=1` option, the source is modelled as a single extended object rather than decomposed into multiple sources. Fig. 4

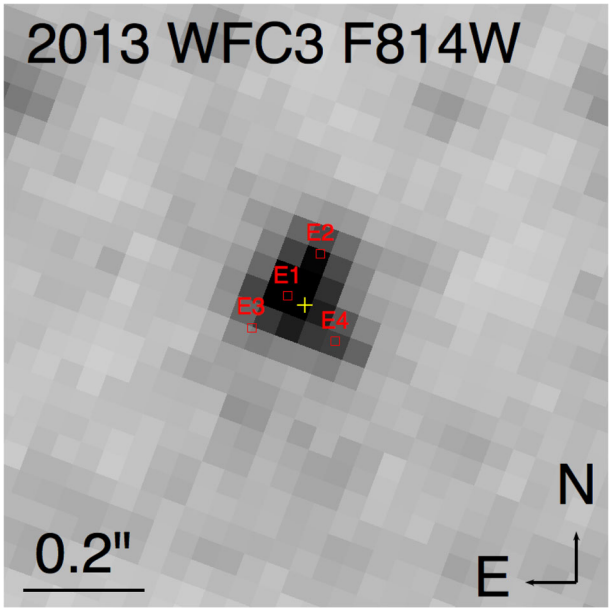

Figure 5. WFC3 *F814W* image (1.0 arcsec^2, north up) from 2013 centred on the estimated position of ASASSN-16fq (yellow cross). The labelled red squares show the positions of DOLPHOT sources reported in Table 1 where the central source (E1) is the brightest.

shows the relevant region of each ACS image and how it has been decomposed into the sources reported in Table 1. The HSC magnitudes agree well (∼0.1 mag) with our results for the *F435W*, *F555W* and *F658N* filters. The difference is much larger for *F814W*, where DOLPHOT has found two sources (D1 and D2) of similar flux. The summed flux of these two sources, corresponding to 22.74 mag, agrees with the HSC flux.

We also analysed the WFC3 images with DOLPHOT, where these are the images that best sample the PSF (0.04 arcsec pixels rather than the 0.05 arcsec scale of ACS) and likely produce the most reliable source decomposition. We identified the sources on the *F814W* image and then obtained photometry for the *F555W* and *F814W* images simultaneously. The sources identified by DOLPHOT are shown in Fig. 5 and their measured magnitudes are reported in Table 1. The position of ASASSN-16fq was again determined by aligning the WFC3 *F814W* image to the ACS *F814W* image.

The photometry reported in Table 1 is not fully consistent given the reported uncertainties. This is not very surprising given that the source appears to be a blend of multiple sources with a decomposition that is not unique under changes in the instrument, camera and filter. We tested running DOLPHOT simultaneously on the ACS and WFC3 *F814W* images, using a single drizzled WFC3 image for source detection. We found systematic offsets of 0.1–0.2 mag between sources as measured on the ACS and WFC3 images. For isolated point sources, the differences should be much smaller (a few times 0.01 mag in tests with SYNPHOT). However, even with the source positions fixed, the flux estimates for the blended sources likely depend in detail on the sub-pixel scale model of the PSF in each frame.

We again used difference imaging to search for evidence that the differences between the ACS and WFC3 magnitudes could be explained by variability. We focused on the *F814W* filter, where a red supergiant exploding as a Type II SN should contribute the most flux. As shown in Fig. 6, there are no significant residuals after using HOTPANTS to scale and subtract the two images. As with the similar test on the WFCP2 *F606W* images above, there is no evidence in the difference image for any variability.

We also searched the archival *Spitzer* data for sources related to the progenitor following the procedures of Khan et al. (2015b). We used the ISIS (Alard & Lupton 1998) difference imaging package to align the *Spitzer* images of a sub-region centred on ASASSN-16fq. Many of the images had an artefact passing close to the SN, so we combined the epochs either missing the artefact or where the artefact avoids its location to build a reference image. We then produced differenced images to search for variability. We also differenced the 3.5 and 4.5 μm reference images to search for dusty stars. In such a 'wavelength difference' image, the normal stars all vanish to leave only stars with significant hot dust emission because they all have a common 'Rayleigh–Jeans' spectral energy distribution (SED; Khan et al. 2010). We found no evidence for mid-IR variability or hot dust emission. There is no mid-IR source at the position of the progenitor. Our best estimates of the 3σ upper limits on the 3.6, 4.5, 5.8 and 8.0 μm fluxes of any source at the position of the progenitor are 15.9, 15.7, 13.3 and 11.4 mag, respectively. The shorter wavelength limits correspond to $\nu L_\nu \lesssim 10^5\,L_\odot$ (at 1σ), and provide no strong constraints given the *HST* photometry.

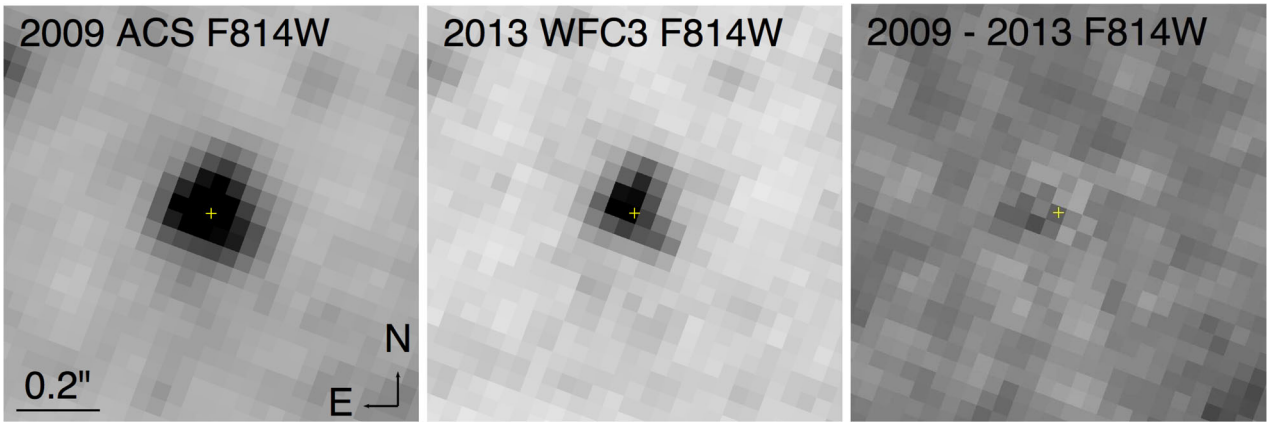

Figure 6. No evidence for variability at *F814W*. The 1.0 arcsec^2 (north up) panels show the ACS (left-hand panel) and WFC3 (middle panel) *F814W* images from 2009 and 2013, respectively, along with the HOTPANTS difference image (right-hand panel) between them. The position of the progenitor candidate for ASASSN-16fq is marked with a yellow cross in all three panels. In the difference image, sources that are brighter in the ACS image appear dark, while those that are brighter in the WFC3 image appear white.

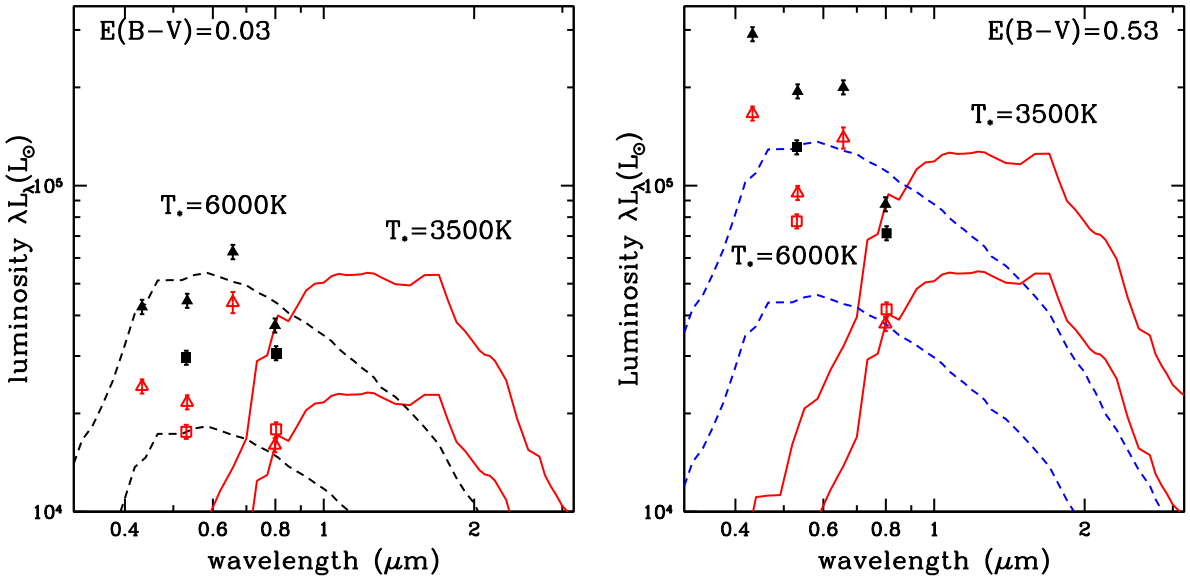

Figure 7. SEDs with low ($E(B-V) = 0.03$, left-hand panel) and high ($E(B-V) = 0.53$, right-hand panel) extinction. The open (filled) squares show the WFC3 photometry for the brightest source (total of all sources) in Table 1. The open (filled) triangles show the ACS photometry for the brightest source (total of all sources) in Table 1. The solid red (dashed blue) curves show the $T_* = 3500$ K ($T_* = 6000$ K) stellar SEDs with the lowest and highest luminosities that fit one of the broad-band photometric points and do not significantly exceed the brightest, total broad-band fluxes (the total ACS fluxes for the broad-band filters).

Clearly with the source blending and the differences between the results for the various cameras, we cannot precisely determine the properties of the progenitor or the amount of extinction. Our goal is simply to provide constraints on the progenitor luminosity that can be translated into rough constraints on the stellar mass. ASASSN-16fq is a Type IIP SN, and all progenitors of Type IIP SN with constrained stellar temperatures have been red supergiants (see Smartt 2015) with stellar temperatures of the order of $T_* = 3500$ K. Higher temperatures of the order of $T_* = 6000$ K have been observed for the progenitors of Type IIb SNe (e.g. SN 2011dh, Maund et al. 2011). Finally, we must note the still higher temperature progenitor of the Type IIpec SN 1987A, a blue supergiant with $T_* \simeq 16\,000$ K and $L_* \simeq 10^{5.0}\,L_\odot$ (see the review by Arnett et al. 1989). All available evidence is that ASASSN-16fq is a normal Type IIP SN where we should only consider the lowest temperature ($T_* = 3500$ K), but we will present parallel results for $T_* = 6000$ K and comment on the consequences of still higher progenitor temperatures.

Rodriguez et al. (2016, in preparation) modelled the early, near-UV/optical/near-IR photometry (from *Swift*, LCOGT 1 m, the Iowa Observatory 0.5 m and the REM 0.6 m) and photospheric expansion velocities of ASASSN-16fq (obtained from optical spectra obtained with FLWO 1.5 m+FAST and MDM 2.4 m+OSMOS) following Pejcha & Prieto (2015). This phenomenological model describes the multicolour light curves and photospheric velocity evolution of normal Type II SNe, decoupling changes in effective temperature from changes in the photospheric radius at different epochs since explosion. These fits lead to an estimated explosion time of JD = 2457532.2 ± 2.0 d, a total extinction (including Galactic) of $E(B-V) = 0.53 \pm 0.02$ mag, and a distance modulus of 29.72 ± 0.44 mag. This distance estimate of 8.8 ± 1.8 Mpc is consistent with our adopted value of 10.62 Mpc. For roughly estimating the properties of the progenitor, we will assume either Galactic $E(B-V) = 0.03$ or $E(B-V) = 0.53$ of foreground extinction. The results assuming circumstellar extinction would be moderately different (see Kochanek et al. 2012b for a discussion of this issue).

We corrected the photometry for the assumed amount of foreground extinction and then used the DUSTY dust radiation transport code (Ivezić & Elitzur 1997; Ivezić, Nenkova & Elitzur 1999; Elitzur & Ivezić 2001) combined with Castelli & Kurucz (2004) model atmospheres of solar metallicity and embedded in a Markov chain Monte Carlo driver to match the model to the data (see Adams & Kochanek 2015; Adams et al. 2016a for details). For the experiments we carry out here, much of this machinery is not necessary but can be trivially applied to the problem. Following Taddia et al. (2015), we estimate that the metallicity at the radius of ASASSN-16fq in M66 should be slightly sub-solar (−0.2 dex). This is not an important change given the crude limits we will derive, particularly since we do not attempt to fit the photometric colours.

For a fixed stellar temperature and foreground extinction, we determined the stellar luminosity based on one of the broad-band ACS or WFC3 total or brightest component magnitudes. The brightest, total broad-band magnitudes (those from ACS) were used as 1σ upper limits on the luminosity unless the magnitude was being used to determine the luminosity. In essence, we will not attempt to extract any colour information from the photometry, but no model can be significantly brighter than the brightest observed ACS/WFC3 broad-band magnitudes.

Fig. 7 shows the 'SED' of the source combining the ACS and WFC3 photometry. All else being equal and ignoring the narrow-band *F658N* photometry, the luminosity estimate will vary by roughly a factor of 2 between a model based on the fluxes of the brightest components (A1-E1) and the summed fluxes of all the components. For example, using $T_* = 3500$ K and Galactic extinction, only models normalized at *I* band (*F814W*) are also consistent with the relevant upper limits. They have luminosities in the range from $L_* = 10^{4.5}$ to $10^{4.9}\,L_\odot$. Essentially, the cool models are too luminous for the observed *F814W* fluxes if they are normalized at shorter wavelengths. For the hotter $T_* = 6000$ K model, all permutations are allowed, and they have luminosities spanning a very similar range from $L_* = 10^{4.5}$ to $10^{4.8}\,L_\odot$. At the hotter

temperature, the stellar SED is not dropping rapidly in the bluer bands and so it is easier to be consistent with all the constraints. When we raise the extinction to $E(B-V) = 0.53$, the changes in the results are modest. For $T_* = 3500$ K, only the *F814W* normalizations are again allowed but with a shift to moderately higher luminosities of $10^{4.8}$–$10^{5.2}$ $L_\odot$. For $T_* = 6000$ K, the *F814W* and *F555W* normalizations are allowed and they have the same luminosity range as for the $T_* = 3500$ K models.

A hot star, albeit one still hotter than the progenitor of SN 1987A, might also explain the discrepant *F658N* magnitudes as H α emission from an associated H II region. With the large $E(B-V) = 0.53$ extinction correction, the implied SED also rises rapidly to shorter wavelengths as might be expected for a hot star. Since the SED rises rapidly to shorter wavelengths, these hot star models are very luminous, with $L_* = 10^{5.5}$–$10^{6.0}$ $L_\odot$ for $T_* = 16\,000$ K and still higher luminosities for higher temperatures. We will not consider this possibility further, although it would make ASASSN-16fq a unique and fascinating new example of the SN phenomenon were it to prove to be true.

If we use the endpoints of the PARSEC (Bressan et al. 2012) isochrones to map luminosities into masses, luminosities of $L_* = 10^{4.5}$, $10^{4.8}$, $10^{4.9}$ and $10^{5.2}$ $L_\odot$ translate into initial masses of $M_* \simeq 8.6$, 11.2, 11.6 and 17 $M_\odot$. Since the higher luminosity limits correspond to the cases normalized by the total flux of all the detected sources rather than just that of the brightest source found by DOLPHOT, they should probably be treated as upper limits. Identifying the brightest sub-component as the progenitor seems probable because the fainter sub-components would have masses inconsistent with becoming a ccSN (i.e. the lower mass limit must be $\gtrsim 8$ $M_\odot$ independent of the photometry). In short, despite the chaotic nature of the photometry, the progenitor of ASASSN-16fq was probably a red supergiant with an initial mass of 8–12 $M_\odot$. This estimate of the mass range is fairly robust to changes in temperature, unless the star is significantly hotter than expected ($T_* > 6000$ K), and holds for a fairly broad range of extinctions. It probably does require that some of the blended stars are significantly hotter and bluer, which would be natural if they are also younger.

3 LBT AND THE VARIABILITY OF THE PROGENITOR

As part of the LBT search for failed SN (Kochanek et al. 2008; Gerke et al. 2015; Adams et al. 2016c), M 66 was observed sixteen times in the *U, B, V* and *R* bands between 2008 May 4 and 2016 February 7. M 66 lies on chip 3 of the Large Binocular Camera (Giallongo et al. 2008) images. The LBT data are analysed using the ISIS (Alard & Lupton 1998) difference imaging package. First, all the images are aligned to a common *R*-band astrometric reference image. The best images (noise, resolution and quality) for each band are combined to make a reference image. These reference images are astrometrically and photometrically calibrated based on SDSS stars (Pier et al. 2003; Ivezić et al. 2007; Ahn et al. 2012) with the SDSS ugriz photometry transformed to *UBVR* Vega magnitudes using the relations in Jordi, Grebel & Ammon (2006). The reference images are then subtracted from the individual epochs to leave only the variable flux between the reference image and the individual epochs. Since the reference image is constructed from images spanning the monitoring period, source fluxes in the reference image roughly correspond to the mean fluxes.

We cannot measure the absolute flux of the progenitor in the LBT images due to crowding. However, the subtracted images are not crowded and we can easily constrain the variability of the progenitor.

Table 2. LBT *R*-band variability.

Date	MJD	ΔL_R ($L_\odot$)
2008-05-04	54590.24	184 ± 1236
2009-01-30	54861.34	−2977 ± 1553
2009-03-22	54912.25	−2335 ± 1641
2010-12-13	55543.44	−1771 ± 1570
2012-01-01	55927.44	−1068 ± 1010
2012-03-22	56008.26	−221 ± 987
2012-04-28	56045.18	3041 ± 1132
2013-03-16	56367.29	−228 ± 1176
2013-05-05	56417.21	330 ± 872
2014-01-09	56666.36	549 ± 1273
2014-04-25	56772.20	−371 ± 734
2015-01-19	57041.32	−571 ± 1323
2015-04-20	57132.23	1604 ± 975
2016-01-03	57390.44	−80 ± 1064
2016-02-07	57425.29	496 ± 1116

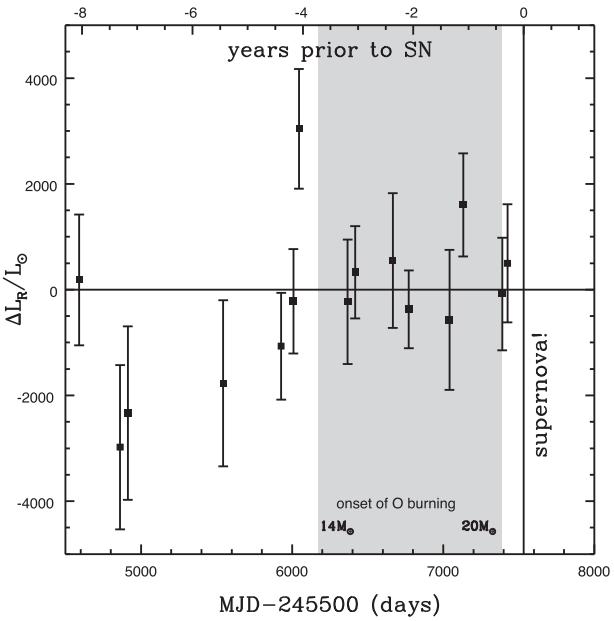

Figure 8. *R*-band progenitor variability prior to the SN relative to the error-weighted mean. The luminosities are not corrected for extinction. The grey band shows the times for the commencement of core oxygen burning for stars with initial mass of 14 $M_\odot$ (left-hand edge) to 20 $M_\odot$ (right-hand edge) from Sukhbold & Woosley (2014). We use these masses because they correspond to the earliest and latest oxygen burning onset times for any star in the model sequence of Fig. 1 that will explode as a red supergiant. For technical reasons, these model sequences were not extended below 12 $M_\odot$. See Fig. 1 for the full mass dependence.

For this purpose, the uniformity of the data and the well-sampled PSF makes the ground-based LBT data superior to the archival *HST* data. Although variability is seen in none of the bands, we focus only on the *R*-band data that are both deeper and of higher quality. Table 2 provides the difference in the *R*-band luminosity relative to the error-weighted mean of all the epochs. The conversion between the *R*-band (νL_ν) luminosity and counts is 3.26 $L_\odot$ count^{-1}, and no correction for extinction has been applied.

As seen in Fig. 8 and Table 2, there is no statistically significant evidence for variability from the progenitor. The rms of the variability is 1505 $L_\odot$ as compared to a mean square uncertainty of 1204 $L_\odot$. Subtracting in quadrature, this implies variability at

Table 3. Progenitor variability.

SN	Time (yr)	Burning phase	rms (mag)	⟨Err⟩ (mag)	Var (mag)	Slope (mag yr^{-1})	χ^2/dof	Reference
SN 1987a	91–33	C Shell	0.3	?	?	0.005 ± ??	–	Plotkin & Clayton (2004)
SN 1993J	9.2–8.8	C Shell	0.17	0.16	0.05	−0.08 ± 0.25	53.3/49	Cohen et al. (1995)
SN 2008cn	12.0–10.8	C Shell	0.22	0.13	0.18	−0.29 ± 0.10	14.2/ 7	Elias-Rosa et al. (2009)
			0.13	0.16	0	−0.03 ± 0.12	6.1/ 7	Maund et al. (2015)
SN 2011dh	3.2–0.1	C→O Shell	0.046	0.022	0.040	0.039 ± 0.006	6.7/ 9	Szczygieł et al. (2012)
SN 2013ej	9.7–8.1	C shell	0.0	0.03	0	0.00 ± 0.026	0.0/ 0	Fraser et al. (2014)
ASASSN-16fq	8.1–0.3	C→O Shell	0.081	0.065	0.049	−0.015 ± 0.008	16.4/13	This paper

an rms level of 900 $L_\odot$. Because the rms is so close to the level of the uncertainties, these should be regarded as upper limits on the variability rather than detections. If we fit a linear trend, the slope is (220 ± 133) $L_\odot$ yr^{-1}, with $\chi^2 = 16.4$ for 13 degrees of freedom. If we rescale the uncertainties to make the χ^2 per degree of freedom unity, this becomes (291 ± 149) $L_\odot$ yr^{-1}. If we adopt an R-band luminosity of $\nu L_\nu = 10^{4.3}\,L_\odot$, the rms variability is <4.5 per cent and the limit on the slope is (1.4 ± 0.7) per cent yr^{-1}. This luminosity estimate is the logarithmic average of the Galactic extinction-corrected ACS and WFC *F814W* and *F555W* C1, D1 and E1 source luminosities. The absolute scale of these luminosities is subject to distance uncertainties and extinction corrections, but the fractional variability is independent of both.

Fig. 8 shows the relation of the LBT epochs to nuclear burning phases with a grey band bracketing the onset of core oxygen burning for models with $14 < M < 20\,M_\odot$ from Sukhbold & Woosley (2014), where the full mass dependence is shown in Fig. 1. We picked 14 and 20 $M_\odot$ because they have the earliest and latest onset times for oxygen burning of the stars that will explode as red supergiants. More or less independent of mass, the LBT data sample the last phases of carbon shell burning, the neon burning phase (not shown), core oxygen burning and the initial phases of shell oxygen burning. Since the two points that drive the apparent slope in the luminosity evolution probably lie in the shell carbon burning phase, the variability in the later burning phases is limited to be even smaller than the overall limits given above.

4 DISCUSSION

We have clearly identified a counterpart to ASASSN-16fq in the archival *HST* data. Unfortunately, our constraints on the properties of the progenitor are far from satisfactory, presumably due to the blending of multiple stars with the progenitor even at the resolution of *HST*. However, for a broad range of reasonable assumptions about its temperature and the amount of extinction, its properties are consistent with a lower mass (8–12 $M_\odot$) red supergiant. The data almost certainly require an upper mass limit of $M_* \lesssim 17\,M_\odot$, which matches the mass limit associated with the red supergiant problem (Smartt et al. 2009) or the more general problem of missing higher mass SN progenitors originally identified by Kochanek et al. (2008). The only real escape from this conclusion is to give the progenitor a far higher than expected temperature, but this option quickly drives the progenitor luminosity to be extraordinarily high. While we view this possibility as unlikely, it would make the progenitor of ASASSN-16fq far more remarkable than simply making it a garden-variety red supergiant of modest mass. Observations either with the LBT or *HST* once the SN has faded will have no difficulty making accurate photometric measurements of the progenitor.

Table 3 summarizes the available information on the variability of SN progenitors beyond the large outbursts probed by Ofek et al. (2014), Bilinski et al. (2015) and Strotjohann et al. (2015). Information is available for the Type IIpec SN 1987A (photographic, Plotkin & Clayton 2004), the Type IIb SN 1993J (V band; Cohen et al. 1995), the Type IIP SN 2008cn (V band; Elias-Rosa et al. 2009; Maund et al. 2015), the Type IIb SN 2011dh (R band; Szczygieł et al. 2012) and the Type IIP SN 2013ej (I band; Fraser et al. 2014) in addition to ASASSN-16fq. Based on the review of Smartt (2009), we adopt progenitor masses of 14–20 $M_\odot$ for SN 1987A and 15 $M_\odot$ for SN 1993J. We use an upper limit of <16 $M_\odot$ for SN 2008cn following Maund et al. (2015), (13 ± 3) $M_\odot$ for SN 2011dh following Maund et al. (2011) and 8–15.5 $M_\odot$ for SN 2013ej (Fraser et al. 2014). We use our estimate of 8–12 $M_\odot$ from Section 2 for ASASSN-16fq. We also report the time period spanned by the variability data and (roughly) the corresponding nuclear burning phases based on Fig. 1. The data for SN 1987A, SN 1993J, SN 2008cn and SN 2013ej probably only sample the carbon shell burning phase. The LBT data for SN 2011dh, like that for ASASSN-16fq, probably samples the last phases of carbon shell burning through the early phases of oxygen shell burning.

We can characterize the 'random', 'steady' and 'outburst' variability of these SN progenitors. Limits on the random variability are illustrated by the 'Var' estimates of the intrinsic variability as a function of the progenitor mass in Fig. 9. The variance 'Var' is estimated by subtracting the mean of the reported photometric uncertainties (⟨Err⟩) from the rms of the light curve, $(\mathrm{Var} = (\mathrm{RMS}^2 - \langle\mathrm{Err}\rangle^2)^{1/2})$. The intrinsic variability is defined to be zero if the mean errors exceed the rms, as is the case for SN 2013ej and the Maund et al. (2015) results for SN 2008cn. These quantities are reported in Table 3. For Fig. 9, we show Var as a limit (just the rms for SN 1987A) unless it exceeds twice the mean uncertainties ⟨Err⟩ (which is only true of SN 2011dh). Limits on the steady variability are illustrated in Fig. 10 by the estimates of the linear luminosity slopes as a function of progenitor mass. The upper limits used for all but SN 2011dh are drawn at the absolute value of the slope plus the error estimate. The slope estimates and the goodness of fit are included in Table 3.

Of these SNe, only SN 2011dh is clearly variable, but with the small number of epochs available to Szczygieł et al. (2012), it is also possible to interpret it as ellipsoidal variability, given the binary models for the progenitor system by Benvenuto, Bersten & Nomoto (2013). For comparison, typical slopes estimated from the end points of stellar evolution models are 10^{-3}–10^{-4} mag yr^{-1} (e.g. Schaller et al. 1992; Heger & Langer 2000). The limit on the slope for SN 1987A is by far the tightest due to the long time-span of the data. Obviously, these systems are heterogeneously selected and sample different final burning phases (see Fig. 1), but they also appear to be the only published progenitors with adequate data to test for these lower levels of variability. Since the existence of the data to test for variability was uncorrelated with any property of the SNe, the sample is actually not a bad proxy for a randomly

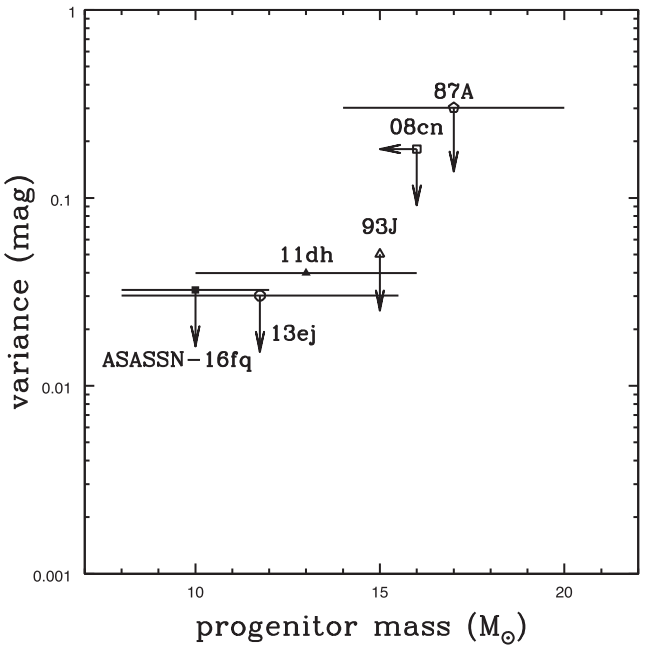

Figure 9. (Left-hand panel) Magnitude variance of the six SN progenitors as a function of their estimated mass. The variance in the progenitor's flux is a measure of any 'random' variability of the progenitor. The time period over which the variance was estimated varies between the SNe (see Fig. 1).

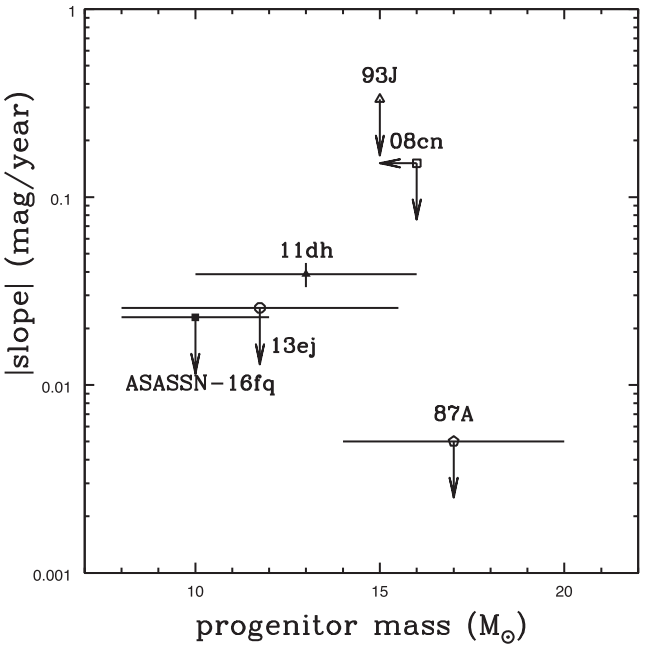

Figure 10. (Right-hand panel) Absolute values of the linear luminosity slopes of the six SN progenitors as a function of their estimated mass. The slope of the progenitor's flux is a measure of any 'steady' variability of the progenitor. For the SN where we have only upper limits, the limit is drawn at the absolute value of the slope plus the uncertainty in the slope. The time period over which the slope was estimated varies between the SNe (see Fig. 1).

selected sample of SNe for simple statistical models despite the heterogeneity of the data.

We can characterize outbursts by adding Gaussian bursts in luminosity (quadratic in magnitude) defined by a peak luminosity $L_{\rm peak}$ and a burst FWHM $t_{\rm peak}$ to the light curves of all the sources in Table 3 except SN 1987A. We allow the outbursts during an eruption time corresponding to the last $t_{\rm out}$ before the SN. We normalize the available light curves to have a χ^2 per degree of freedom, $N_{\rm dof}$, of at most unity (i.e. ignoring the variability of SN 2011dh) when fit as having a constant flux. We then add model outbursts at random times and conservatively define detection to be when the χ^2 for fitting the 'fake' data containing an outburst as having a constant flux exceeds the larger of $2N_{\rm dof}$ and $N_{\rm dof}+4$. Fig. 11 shows the results, quantified as the detection probability per SN, $P_{\rm d}$, for peak outburst luminosities of $M_R=-6$, -8, -10 and -12 mag, corresponding to $\lambda L_\lambda \simeq 10^{4.0}$, $10^{4.8}$ $10^{5.6}$ and $10^{6.4}\,{\rm L}_\odot$. The detection probabilities can then be converted to 90 per cent confidence limits on the number of outbursts per SN as

$$N_{\rm out} < \frac{2.30}{N_{\rm SN}P_{\rm d}} = 0.46P_{\rm d}^{-1}, \quad (1)$$

where $N_{\rm SN}=5$ since we have excluded SN 1987A from the analysis. The rate of eruptions during the eruption period is then $r_{\rm out}=N_{\rm out}/t_{\rm out}$.

The general pattern of the detection probabilities $P_{\rm d}$ in Fig. 11 is relatively easy to understand. Short outbursts become increasingly difficult to detect because of the finite temporal sampling of the data. Long outbursts ultimately become difficult to detect because they show no time variability over the finite temporal extent of the data (although for sufficiently bright transients, the luminosity would be incompatible with any progenitor). The results for long outbursts eventually correspond to the slope limits of Fig. 10. The sensitivity is highest for eruption periods extending to roughly 10 yr because SN 1993J, SN 2008cn and SN 2013ej only contribute on these time-scales. For the shortest eruption periods ($t_{\rm out}$), only SN 2011dh contributes, and for long eruption periods, there is no information outside the last roughly 10 yr before the SN.

Fig. 12 shows outburst limits computed in the same manner for the sample of 27 Type IIb SN considered by Strotjohann et al. (2015) for comparison. Ofek et al. (2014) and Strotjohann et al. (2015) provide 5σ R-band luminosity limits, $L_{\rm PTF}$, for 15 d bins of the data, each containing a variable number, $N_{\rm PTF}$, of epochs. For simplicity, we simply spread the reported number of epochs uniformly over their 15-d bin (with temporal spacings of 1/2: 1: 1. . . 1: 1: 1/2 over the bin), each with a (1σ) uncertainty per epoch of $L_{\rm PTF}N_{\rm PTF}^{1/2}/5$. We can then apply our formalism with only minor ambiguities for very short time-scale ($t_{\rm peak} \lesssim 15$ d) outbursts. Fig. 12 shows the results for the Strotjohann et al. (2015) sample at $M_R=-12$ and -10 mag. The Type IIn sample considered by Ofek et al. (2014) has even less sensitivity to low-luminosity outbursts because the typical SN is more distant and there are fewer SN in the sample.

As we can see from comparing Figs 11 and 12, the PTF sample is more sensitive to very luminous outbursts and far less sensitive to outbursts closer to the progenitor luminosity. This is simply because, relative to the sample in Table 3, the PTF data have more continuous, but very shallow coverage of a larger number of SN. The rate limits of the two samples cross near peak luminosities of $M_R=-12$ mag ($\lambda L_\lambda \simeq 10^{6.4}\,{\rm L}_\odot$), where the relative sensitivity depends on the burst duration. By $M_R=-10$ mag ($\lambda L_\lambda \simeq 10^{5.6}\,{\rm L}_\odot$), the deeper data we use here are more sensitive independent of the outburst duration. The PTF data have negligible sensitivity to the fainter $M_R=-8$ and -6 mag outbursts.

In essence, the two approaches are complimentary. SN surveys like PTF will better constrain the rates of high luminosity, shorter transients – they will generally have larger numbers of SN observed with higher cadence. However, even with the co-addition of data,

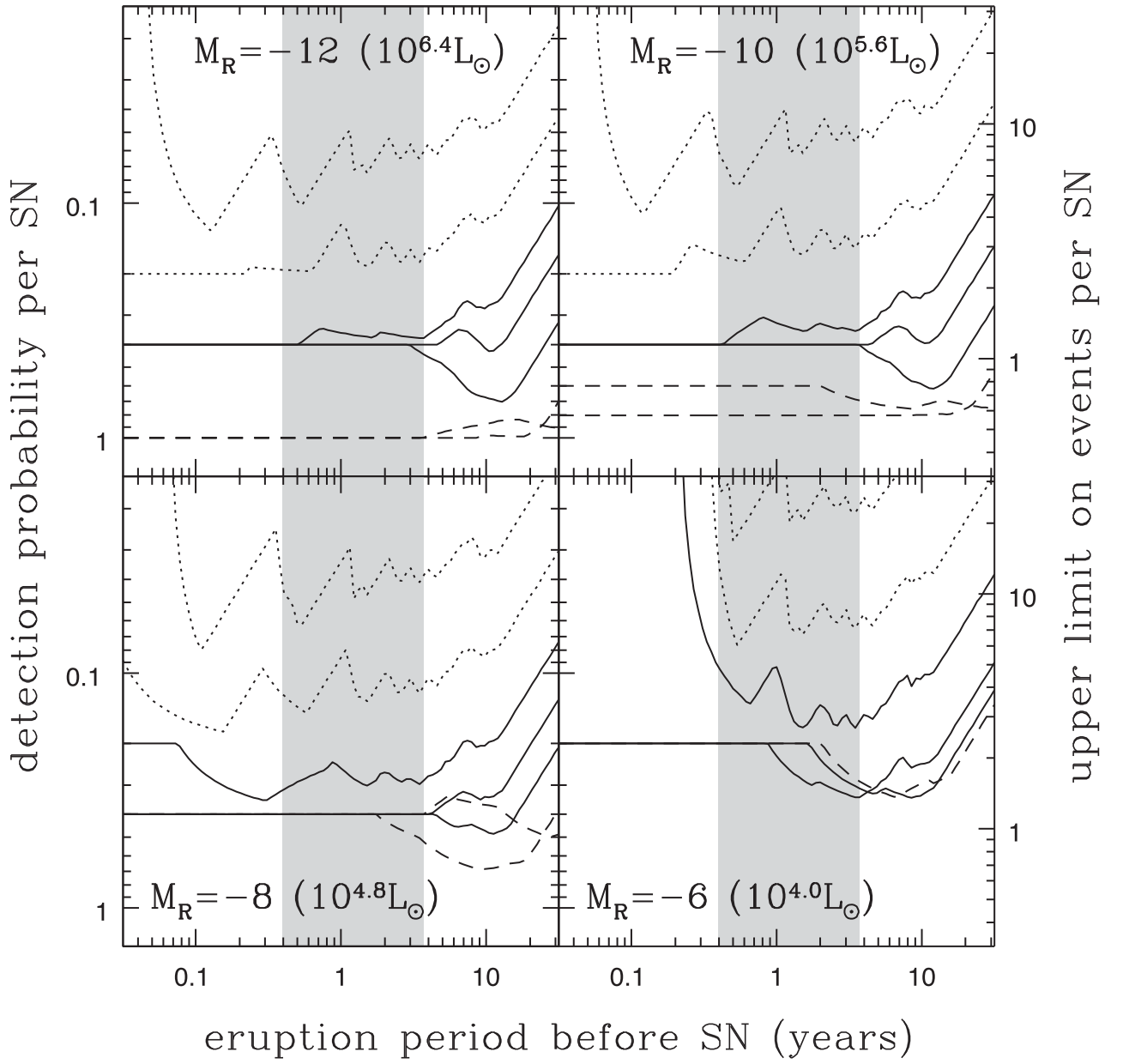

Figure 11. Outburst detection probabilities (P_d, left-hand scale; note that this scale is inverted, with lower probabilities at the top) and 90 per cent confidence upper limits on the number of outbursts per SN (N_{out}, right scale) as a function of the period t_{out} over which eruptions can occur prior to the SN. The panels show the results for different peak luminosities from $M_R = -12$ (top left-hand panel) down to $M_R = -6$ mag (bottom right-hand panel) where the associated luminosities are λL_λ at R band. The curves correspond to logarithmically spaced outburst FWHM of $t_{peak} = 0.032$ (highest, dotted), 0.1 (dotted), 0.32 (solid), 1.0 (solid), 3.2 (solid), 10.0 (dashed) and 32 (usually lowest, dashed) years. As in Fig. 8, the shaded region shows the time before collapse for the onset of core oxygen burning in the 14 and 20 $M_\odot$ models (see Fig. 1). The limit on the number of N_{out} outbursts and the detection probability P_d are related by $N_{out} = 2.3(N_{SN}P_d)^{-1}$ for the $N_{SN} = 5$ SN excluding SN 1987A.

SN surveys simply lack the sensitivity to probe variability significantly below ∼10 times the luminosity of the progenitor stars. Deep monitoring data, like that from our LBT survey, are sensitive to very low levels of variability (down to ∼1 per cent of the progenitor luminosity, Fig. 8), but are limited by the SN rate in nearby galaxies (∼1 year) and the lower cadence of any monitoring project on large telescopes.

SN surveys like PTF are also largely limited to studying the relationships between outburst and SN properties, as done by Ofek et al. (2014), because most of the SN will be too distant for measurements of the progenitor properties. Any survey that can measure variability on the scale of the progenitor luminosity or fainter can, by definition, also determine the properties of the progenitor. As a result, studies like the LBT survey (Kochanek et al. 2008; Gerke et al. 2015; Adams et al. 2016c) are better suited to studying the relationship between outbursts and progenitors. An obvious next step is to systematically analyse the variability of all the SN progenitors in the LBT survey data, which will provide a relatively homogeneous, volume-limited sample, rather than the heterogeneous sample represented by Table 3.

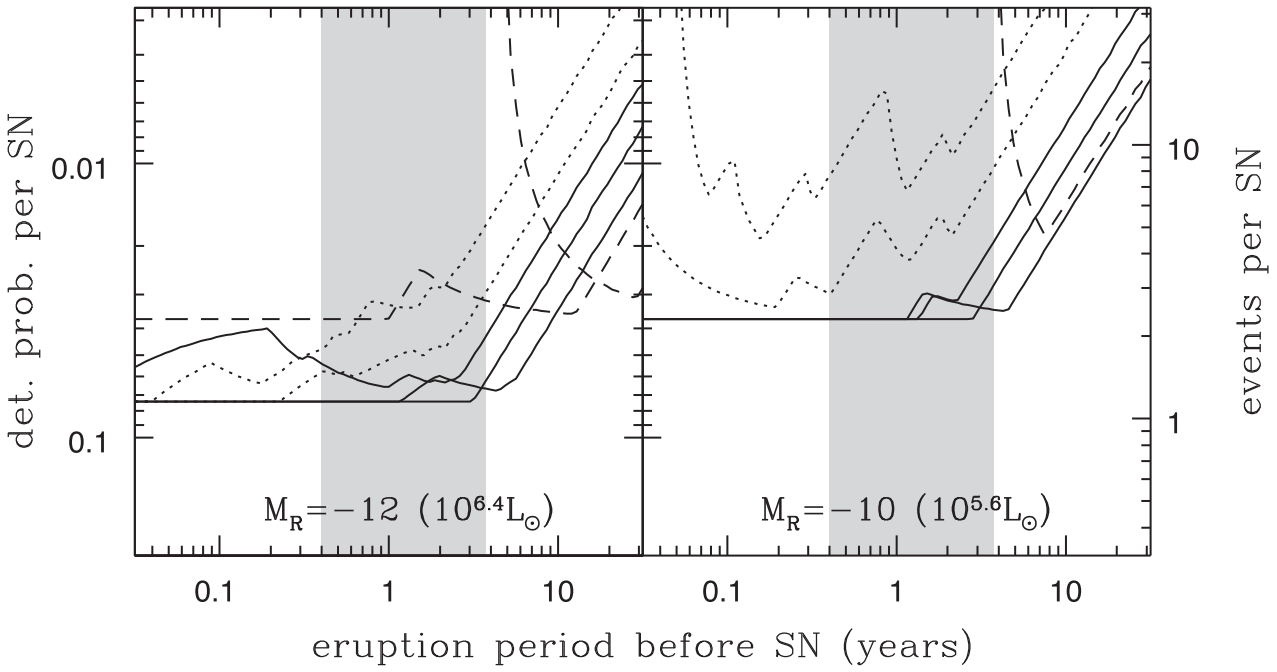

Figure 12. Outburst detection probabilities (left-hand scale; note that this scale is inverted, with lower probabilities at the top) and 90 per cent confidence upper limits on the number of outbursts per SN (right scale) as a function of the period over which eruptions can occur prior to the SN for the PTF data on Type IIb SN progenitors considered by Strotjohann et al. (2015). The format is the same as in Fig. 11, but we only show the results for $M_R = -10$ and -8 mag, where there is some overlap with the sensitivities shown in Fig. 11. The curves correspond to logarithmically spaced outburst FWHM of $t_{peak} = 0.032$ (highest, dotted), 0.1 (dotted), 0.32 (solid), 1.0 (solid), 3.2 (solid), 10.0 (dashed) and 32 (usually lowest, dashed) years. The PTF sample is better for brighter transients (more SN with better temporal coverage) and worse for fainter transients (insufficient depth). As in Fig. 8, the shaded region shows the time before collapse for the onset of core oxygen burning in the 14 and 20 $M_\odot$ models (see Fig. 1). The limit on the number of N_{out} outbursts and the detection probability P_d are related by $N_{out} = 2.3(N_{SN}P_d)^{-1}$ for the $N_{SN} = 27$ SN in the Strotjohann et al. (2015) sample.

ACKNOWLEDGEMENTS

We thank A. Dolphin for his advice regarding DOLPHOT. CSK, KZS, JSB, SMA and TWSH are supported by NSF grants AST-1515876 and AST-1515927. BJS is supported by NASA through Hubble Fellowship grant HF-51348.001 awarded by the Space Telescope Science Institute, which is operated by the Association of Universities for Research in Astronomy, Inc., for NASA, under contract NAS 5-26555. TW-SH is supported by the DOE Computational Science Graduate Fellowship, grant number DE-FG02- 97ER25308. TS is partly supported by NSF grant PHY-1404311 to J. Beacom. This work was partly supported by the European Union FP7 programme through ERC grant number 320360. Support for JLP is provided in part by FONDECYT through the grant 1151445 and by the Ministry of Economy, Development, and Tourism's Millennium Science Initiative through grant IC120009, awarded to The Millennium Institute of Astrophysics, MAS. SD is supported by the Strategic Priority Research Program 'The Emergence of Cosmological Structures' of the Chinese Academy of Sciences (Grant No. XDB09000000) and NSFC project 11573003. Some of the observations were carried out using the LBT at Mt Graham, AZ. The LBT is an international collaboration among institutions in the United States, Italy and Germany. LBT Corporation partners are the University of Arizona on behalf of the Arizona university system; Istituto Nazionale di Astrofisica, Italy; LBT Beteiligungsgesellschaft, Germany, representing the Max–Planck Society, the Astrophysical Institute Potsdam and Heidelberg University; the Ohio State University; and The Research Corporation, on behalf of the University of Notre Dame, University of Minnesota and University of Virginia. This work is based in part on observations made with the *Spitzer Space Telescope*, which is operated by the Jet Propulsion Laboratory, California Institute of Technology under a contract with NASA, and in part on observations made with the NASA/ESA *HST* obtained at the Space Telescope Institute, which is operated by the Association of Universities for Research in Astronomy, Inc., under NASA contract NAS 5-26555. Some observations were obtained from the Hubble Legacy Archive, which is a collaboration between the Space Telescope Science Institute (STScI/NASA), the Space Telescope European Coordinating Facility (ST-ECF/ESA) and the Canadian Astronomy Data Centre (CADC/NRC/CSA).

REFERENCES

Abbott B. P. et al., 2016, Phys. Rev. Lett., 116, 061102
Adams S. M., Kochanek C. S., 2015, MNRAS, 452, 2195
Adams S. M., Kochanek C. S., Prieto J. L., Dai X., Shappee B. J., Stanek K. Z., 2016a, MNRAS, 460, 1645
Adams S. M., Kochanek C. S., Gerke J. R., Stanek K. Z., Dai X., 2016b, MNRAS, preprint (arXiv:1609.01283)
Adams S. M., Kochanek C. S., Gerke J. R., Stanek K. Z., 2016c, MNRAS, preprint (arXiv:1610.02402)
Ahn C. P. et al., 2012, ApJS, 203, 21
Alard C., Lupton R. H., 1998, ApJ, 503, 325
Arnett W. D., Bahcall J. N., Kirshner R. P., Woosley S. E., 1989, ARA&A, 27, 629
Belczynski K., Holz D. E., Bulik T., O'Shaughnessy R., 2016, Nature, 534, 512
Benvenuto O. G., Bersten M. C., Nomoto K., 2013, ApJ, 762, 74
Bilinski C., Smith N., Li W., Williams G. G., Zheng W., Filippenko A. V., 2015, MNRAS, 450, 246
Bock G. et al., 2016, Astron. Telegram, 9091

Bressan A., Marigo P., Girardi L., Salasnich B., Dal Cero C., Rubele S., Nanni A., 2012, MNRAS, 427, 127
Brown J. M., Woosley S. E., 2013, ApJ, 769, 99
Cao Y. et al., 2013, ApJ, 775, L7
Castelli F., Kurucz R. L., 2004, preprint (arXiv:astro-ph/0405087)
Clausen D., Piro A. L., Ott C. D., 2015, ApJ, 799, 190
Cohen J. G., Darling J., Porter A., 1995, AJ, 110, 308
Couch S. M., Ott C. D., 2015, ApJ, 799, 5
Dalcanton J. J. et al., 2009, ApJS, 183, 67
Dolence J. C., Burrows A., Zhang W., 2015, ApJ, 800, 10
Dolphin A. E., 2000, PASP, 112, 1383
Eldridge J. J., Fraser M., Smartt S. J., Maund J. R., Crockett R. M., 2013, MNRAS, 436, 774
Elias-Rosa N. et al., 2009, ApJ, 706, 1174
Elias-Rosa N. et al., 2011, ApJ, 742, 6
Elitzur M., Ivezić Ž., 2001, MNRAS, 327, 403
Ertl T., Janka H.-T., Woosley S. E., Sukhbold T., Ugliano M., 2016, ApJ, 818, 124
Filippenko A. V., 1997, ARA&A, 35, 309
Folatelli G. et al., 2016, ApJ, 825, L22
Foley R. J., Berger E., Fox O., Levesque E. M., Challis P. J., Ivans I. I., Rhoads J. E., Soderberg A. M., 2011, ApJ, 732, 32
Fraser M. et al., 2012, ApJ, 759, L13
Fraser M. et al., 2013, ApJ, 779, L8
Fraser M. et al., 2014, MNRAS, 439, L56
Gal-Yam A., 2012, Science, 337, 927
Gerke J. R., Kochanek C. S., Stanek K. Z., 2015, MNRAS, 450, 3289
Giallongo E. et al., 2008, A&A, 482, 349
Groh J. H., Meynet G., Georgy C., Ekström S., 2013, A&A, 558, A131
Heger A., Langer N., 2000, ApJ, 544, 1016
Horiuchi S., Beacom J. F., Kochanek C. S., Prieto J. L., Stanek K. Z., Thompson T. A., 2011, ApJ, 738, 154
Humphreys R. M., Davidson K., 1994, PASP, 106, 1025
Ivezić Z., Elitzur M., 1997, MNRAS, 287, 799
Ivezić Z., Nenkova M., Elitzur M., 1999, preprint (arXiv:astro-ph/9910475)
Ivezić, Ž.et al., 2007, AJ, 134, 973
Jennings Z. G., Williams B. F., Murphy J. W., Dalcanton J. J., Gilbert K. M., Dolphin A. E., Weisz D. R., Fouesneau M., 2014, ApJ, 795, 170
Jerkstrand A., Smartt S. J., Fraser M., Fransson C., Sollerman J., Taddia F., Kotak R., 2014, MNRAS, 439, 3694
Jordi K., Grebel E. K., Ammon K., 2006, A&A, 460, 339
Kanbur S. M., Ngeow C., Nikolaev S., Tanvir N. R., Hendry M. A., 2003, A&A, 411, 361
Khan R., Stanek K. Z., Prieto J. L., Kochanek C. S., Thompson T. A., Beacom J. F., 2010, ApJ, 715, 1094
Khan R., Kochanek C. S., Stanek K. Z., Gerke J., 2015a, ApJ, 799, 187
Khan R., Adams S. M., Stanek K. Z., Kochanek C. S., Sonneborn G., 2015b, ApJ, 815, L18
Kiewe M. et al., 2012, ApJ, 744, 10
Kochanek C. S., 2011, ApJ, 743, 73
Kochanek C. S., 2014, ApJ, 785, 28
Kochanek C. S., 2015, MNRAS, 446, 1213
Kochanek C. S., Beacom J. F., Kistler M. D., Prieto J. L., Stanek K. Z., Thompson T. A., Yüksel H., 2008, ApJ, 684, 1336
Kochanek C. S., Szczygieł D. M., Stanek K. Z., 2012a, ApJ, 758, 142
Kochanek C. S., Khan R., Dai X., 2012b, ApJ, 759, 20
Li W., Van Dyk S. D., Filippenko A. V., Cuillandre Jean-Charles, Jha S., Bloom J. S., Riess A. G., Livio M., 2006, ApJ, 641, 1060
Lien A., Fields B. D., Beacom J. F., 2010, Phys. Rev. D, 81, 083001
Margutti R. et al., 2014, ApJ, 780, 21
Mauerhan J. C. et al., 2013, MNRAS, 430, 1801
Maund J. R. et al., 2011, ApJ, 739, L37
Maund J. R., Fraser M., Reilly E., Ergon M., Mattila S., 2015, MNRAS, 447, 3207
Müller B., 2016, Publ. Astron. Soc. Aust., 33, e048
O'Connor E., Ott C. D., 2013, ApJ, 762, 126
Ofek E. O. et al., 2014, ApJ, 789, 104
Ofek E. O. et al., 2016, ApJ, 824, 6
Pastorello A. et al., 2007, Nature, 447, 829
Pastorello A. et al., 2013, ApJ, 767, 1
Pejcha O., Prieto J. L., 2015, ApJ, 799, 215
Pejcha O., Thompson T. A., 2015, ApJ, 801, 90
Pier J. R., Munn J. A., Hindsley R. B., Hennessy G. S., Kent S. M., Lupton R. H., Ivezic Z., 2003, AJ, 125, 1559
Plotkin R. M., Clayton G. C., 2004, JAAVSO, 32, 89
Quataert E., Shiode J., 2012, MNRAS, 423, L92
Reynolds T. M., Fraser M., Gilmore G., 2015, MNRAS, 453, 2885
Sana H. et al., 2012, Science, 337, 444
Schaller G., Schaerer D., Meynet G., Maeder A., 1992, A&AS, 96, 269
Schlafly E. F., Finkbeiner D. P., 2011, ApJ, 737, 103
Shappee B. J. et al., 2014, ApJ, 788, 48
Shiode J. H., Quataert E., 2014, ApJ, 780, 96
Smartt S. J., 2009, ARA&A, 47, 63
Smartt S. J., 2015, Publ. Astron. Soc. Aust., 32, e016
Smartt S. J., Maund J. R., Hendry M. A., Tout C. A., Gilmore G. F., Mattila S., Benn C. R., 2004, Science, 303, 499
Smartt S. J., Eldridge J. J., Crockett R. M., Maund J. R., 2009, MNRAS, 395, 1409
Smith N., 2014, ARA&A, 52, 487
Smith N., Arnett W. D., 2014, ApJ, 785, 82
Smith N., McCray R., 2007, ApJ, 671, L17
Smith N. et al., 2010, AJ, 139, 1451
Smith N., Li W., Silverman J. M., Ganeshalingam M., Filippenko A. V., 2011, MNRAS, 415, 773
Strotjohann N. L. et al., 2015, ApJ, 811, 117
Sukhbold T., Woosley S. E., 2014, ApJ, 783, 10
Sukhbold T., Ertl T., Woosley S. E., Brown J. M., Janka H.-T., 2016, ApJ, 821, 38
Szczygieł D. M., Gerke J. R., Kochanek C. S., Stanek K. Z., 2012, ApJ, 747, 23
Taddia F. et al., 2015, A&A, 580, A131
Tinyanont S. et al., 2016, ApJ, 833, 231
Ugliano M., Janka H.-T., Marek A., Arcones A., 2012, ApJ, 757, 69
Van Dyk S. D., Peng C. Y., King J. Y., Filippenko A. V., Treffers R. R., Li W., Richmond M. W., 2000, PASP, 112, 1532
Van Dyk S. D., Li W., Filippenko A. V., 2003, PASP, 115, 1289
Van Dyk S. D. et al., 2011, ApJ, 741, L28
Walmswell J. J., Eldridge J. J., 2012, MNRAS, 419, 2054
Whitmore B. C. et al., 2016, AJ, 151, 134
Wongwathanarat A., Müller E., Janka H.-T., 2015, A&A, 577, A48
Woosley S. E., 2016, ApJ, 824, L10
Woosley S. E., Heger A., 2007, Phys. Rep., 442, 269
Woosley S. E., Heger A., 2015, ApJ, 810, 34
Zhang J., Zheng X., Wang X., Rui L., 2016, Astron. Telegram, 9093

This paper has been typeset from a TEX/LATEX file prepared by the author.